

# Rapid three-dimensional isotropic imaging of living cells using Bessel beam plane illumination

Thomas A Planchon<sup>1,6</sup>, Liang Gao<sup>1,6</sup>, Daniel E Milkie<sup>2</sup>, Michael W Davidson<sup>3</sup>, James A Galbraith<sup>4</sup>, Catherine G Galbraith<sup>5</sup> & Eric Betzig<sup>1</sup>

**A key challenge when imaging living cells is how to noninvasively extract the most spatiotemporal information possible. Unlike popular wide-field and confocal methods, plane-illumination microscopy limits excitation to the information-rich vicinity of the focal plane, providing effective optical sectioning and high speed while minimizing out-of-focus background and premature photobleaching. Here we used scanned Bessel beams in conjunction with structured illumination and/or two-photon excitation to create thinner light sheets (<0.5  $\mu\text{m}$ ) better suited to three-dimensional (3D) subcellular imaging. As demonstrated by imaging the dynamics of mitochondria, filopodia, membrane ruffles, intracellular vesicles and mitotic chromosomes in live cells, the microscope currently offers 3D isotropic resolution down to  $\sim 0.3 \mu\text{m}$ , speeds up to nearly 200 image planes per second and the ability to noninvasively acquire hundreds of 3D data volumes from single living cells encompassing tens of thousands of image frames.**

A common theme in modern biological fluorescence microscopy is the quest to extract ever more information from a single cell, whether by higher spatial<sup>1</sup>, temporal<sup>2</sup> or spectral<sup>3</sup> resolution. As spatial resolution improves, each three-dimensional (3D) voxel encompasses fewer fluorescent molecules (Fig. 1a). In live-cell imaging, as temporal resolution improves, fewer molecules in each voxel can be sacrificed to fluorescence photobleaching in each 3D image stack (Fig. 1b). In short, the photon budget for each voxel at each point in time becomes increasingly constrained as spatiotemporal resolution improves. In contrast, photon statistics also demand that a minimum number of photons  $N$  be collected from each voxel at each time point to yield images of acceptable signal-to-noise ratio (SNR),  $N^{1/2}$  (Fig. 1c). Thus, as the quest for higher spatiotemporal resolution continues, it becomes imperative to devise methods to spend the photon budget wisely.

Unfortunately, many common methods of fluorescence microscopy (wide-field, structured illumination, 3D photoactivated localization, confocal and stimulated emission depletion microscopy) use an epi-illumination configuration that exposes

the entire sample thickness to the illuminating radiation. As high-resolution information is obtained only from the vicinity of the focal plane of the detection objective, with these methods the photon budget is increasingly wasted for increasingly thick samples. For live cells, the phototoxic effects of whole-cell illumination can prove even more limiting to physiological studies than photobleaching itself<sup>4</sup>.

A notable exception is plane-illumination microscopy<sup>5</sup>, which uses a separate excitation lens orthogonal to the detection objective to confine the excitation close to the focal plane of the latter. Although this has been successful for imaging large multicellular organisms at single-cell resolution<sup>6,7</sup>, a tradeoff exists between the minimum thickness of the light sheet and the field of view over which it remains reasonably uniform such that, when imaging a 50- $\mu\text{m}$ -diameter cultured cell, an optimized Gaussian light sheet diverges to a full-width at half-maximum (FWHM) thickness of 2.8  $\mu\text{m}$  at either end. As this is threefold greater than the depth of focus of a high-numerical-aperture (NA) detection objective, substantial out-of-focus excitation remains, and hence the benefits of background reduction and photobleaching mitigation that are the hallmarks of plane illumination are not fully realized. Furthermore, such light sheets are too thick to aid in improving axial resolution, which is  $\sim 3\text{--}4\times$  poorer than transverse resolution, even when high-NA optics are used.

We describe the use of scanned Bessel beams<sup>8</sup> to generate much thinner light sheets. Bessel beams are created by projecting an annular illumination pattern at the rear pupil of an excitation lens<sup>9</sup>; their central peak width (Supplementary Fig. 1), unlike Gaussian beams, can be decoupled from their longitudinal extent (Supplementary Fig. 2) simply by changing the thickness of the annulus. The self-reconstructing property<sup>10</sup> of such beams has recently been used to reduce shadowing and scattering artifacts in plane illumination microscopy of multicellular organisms<sup>11</sup>. Here we use scanned Bessel beams of higher NA to create light sheets sufficiently thin to achieve isotropic 3D resolution and improve the expenditure of the photon budget to the point at which hundreds of 3D image stacks comprising tens of thousands of frames can be acquired from single living cells at rates of nearly 200 frames  $\text{s}^{-1}$ .

<sup>1</sup>Janelia Farm Research Campus, Howard Hughes Medical Institute, Ashburn, Virginia, USA. <sup>2</sup>Coleman Technologies, Inc., Chadds Ford, Pennsylvania, USA. <sup>3</sup>National High Magnetic Field Laboratory and Department of Biological Science, Florida State University, Tallahassee, Florida, USA. <sup>4</sup>National Institute of Neurological Disorders and Stroke, National Institutes of Health, Bethesda, Maryland, USA. <sup>5</sup>National Institute of Child Health and Human Development, National Institutes of Health, Bethesda, Maryland, USA. <sup>6</sup>These authors contributed equally to this work. Correspondence should be addressed to E.B. (betzige@janelia.hhmi.org).

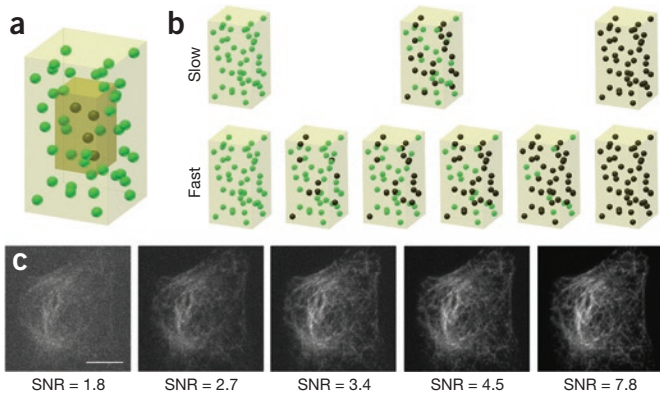


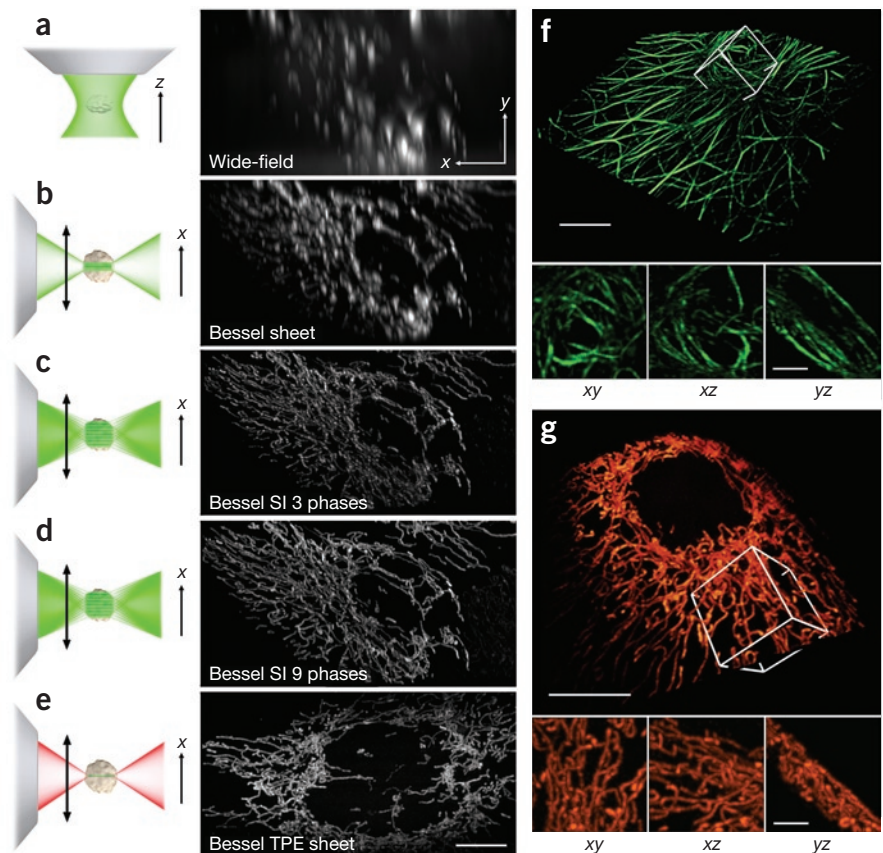
**Figure 1** | Challenges in fluorescence imaging with high spatiotemporal resolution. (a) Increasing volumetric spatial resolution demands smaller voxels (boxes) encompassing fewer signal-generating fluorescent molecules (spheres). (b) Increasing temporal resolution demands that fewer molecules be expended (black spheres) at each time point. (c) To obtain images of acceptable SNR, a certain minimum number of photons must be emitted from these molecules, no matter how few they may be. Scale bar, 5  $\mu\text{m}$ .

## RESULTS

### Bessel beam plane illumination microscopy

Our Bessel beam plane illumination microscope (Supplementary Fig. 3) uses a galvanometer to sweep the circular Bessel beam in the  $x$  direction across the plane of focus of the detection objective to create a scanned light sheet and yield an image at a single  $z$  direction plane in the specimen. To achieve isotropic resolution, we used excitation and detection objectives of equal NA (Supplementary Fig. 4). To produce Bessel beams at such NA

**Figure 2** | Modes of Bessel beam plane illumination microscopy. (a) Wide-field illumination geometry (left) and maximum-intensity projection (MIP) in the  $x$ - $z$  plane (right;  $z$ , detection axis) from a 3D image stack of a fixed human osteosarcoma cell (U2OS) transfected with plasmids encoding mEmerald fused to human pyruvate dehydrogenase alpha 1 (PDHA1). (b) Bessel sheet mode geometry (left), showing fluorescence excitation from Bessel side lobes (light green) as well as the central peak (dark green), and  $x$ - $z$  plane MIP (right) from same cell as in a. (c,d) Bessel SI mode geometry, showing periodic Bessel beam excitation pattern (left) and  $x$ - $z$  plane MIPs with single-harmonic (c) and multiharmonic (d) excitation (right). (e) Two-photon excitation (TPE) Bessel sheet mode geometry (left), showing infrared excitation (red) of fluorescence in the central peak (green), with negligible fluorescence in side lobes and  $x$ - $z$  plane MIP from a cell (right) similar to those in a-d. (f) Volume rendering in the multiharmonic SI mode (9 phases, 2.4  $\mu\text{m}$  period) of mEmerald-tagged microtubule associated protein 4 (MAP4) in a live U2OS cell. (g) Volume rendering in the TPE sheet mode of mEmerald-labeled mitochondria in a live pig kidney epithelial cell (LLC-PK1 cell line). Insets in f and g show MIPs along orthogonal axes of the cubical volumes shown. Scale bars, 10  $\mu\text{m}$  except 3  $\mu\text{m}$  in insets.



sufficiently long to cover the entire cell, we placed an annular apodization mask at a plane conjugate to both the galvanometer and the rear pupil of the excitation objective. Finally, to enable high-speed volumetric imaging without moving the specimen, we used a second galvanometer to increment the position of the scan plane after each image and a piezoelectric collar to translate the detection objective to follow suit (Online Methods).

The simplest mode of operation, akin to that used in the digital scanned laser light sheet fluorescence microscopy<sup>7</sup> (DSLMS), involves sweeping the Bessel beam in the  $x$  direction to create a continuous sheet at each  $z$  plane of a 3D image stack. As expected, this Bessel sheet mode led to less out-of-focus background (Supplementary Fig. 5) than did wide-field illumination. Furthermore,  $x$ - $z$ -plane projections of mitochondria in the same fixed cell (Fig. 2) had improved axial resolution, once the raw data were deconvolved with the appropriate point spread functions (PSFs) (Fig. 2a,b, Supplementary Figs. 6–8 and Online Methods).

Nevertheless, the Bessel sheet mode is not ideal. The problem is that substantial energy resides in the side lobes of a Bessel beam<sup>8</sup> (Supplementary Figs. 1 and 9a). As a result, the cross-sectional profile of the sheet of excitation we created by sweeping the beam contains not only a narrow peak corresponding to the central maximum of the Bessel beam but also broad tails because of the combined influence of the side lobes (Supplementary Fig. 9b). Choosing a thicker annulus suppressed these tails but at the expense of the beam length (Supplementary Fig. 10) and hence the usable field of view, as it becomes more Gaussian in character. Fortunately, the finite depth of focus provided by wide-field detection mitigated the effect of the tails in the overall axial PSF (Supplementary Figs. 7 and 9c). In principle, the central peak extends the axial resolution of the Bessel sheet

mode  $> 4\times$  beyond the wide-field limit, but in practice, the substantial signal from the tails heavily weighted the information in the image toward low axial spatial frequencies  $k_z$  (Supplementary Fig. 11). This made accurate deconvolution at the highest  $k_z$  difficult and thus limited the improvement to the gains shown (Fig. 2b).

### Bessel beam structured plane illumination microscopy

One means to reduce the influence of the side lobes and improve the axial PSF is to use structured illumination (SI)-based optical sectioning. In the standard wide-field implementation<sup>12</sup>, one projects a periodic excitation pattern through an epi-illumination objective to the focal plane and then acquires three images  $I_n$  ( $n = 1, 2$  and  $3$ ) while translating the pattern in steps of one-third period. As the observable amplitude of the pattern decreases as it becomes increasingly out of focus, combining the images into a final image  $I_{\text{final}}$  according to

$$I_{\text{final}} = \left| \sum_{n=1}^N I_n \exp(2\pi i n / N) \right| \quad (1)$$

in which  $i = (-1)^{1/2}$  and  $N$  is the number of images, removes the weakly modulated out-of-focus component and retains the strongly modulated information near the focal plane.

To adopt this approach to Bessel beam plane illumination, we exposed the beam at discrete, periodic points across the entire  $x$  field of view. If the exposure period is larger than the  $\lambda/(2NA_{\text{Bessel max}})$  Abbe limit of the Bessel excitation but smaller than  $\lambda/(NA_{\text{Bessel max}})$ , this generates a resolvable pattern containing a single harmonic (Supplementary Fig. 12). We then acquired three such images, with the pattern in each shifted by one-third period and applied equation (1) to obtain a final image. Both PSF measurements (Supplementary Fig. 13) and cellular images (Fig. 2c) confirmed the predicted result<sup>12</sup> that this single-harmonic, three-image SI mode achieved optimal sectioning (Supplementary Fig. 5) and axial resolution ( $0.27 \mu\text{m}$  FWHM, Supplementary Fig. 8) at a period just below  $\lambda/(NA_{\text{Bessel max}})$ . Indeed, at this period the axial spatial frequencies extended even beyond the diffraction limit of  $\lambda/(2NA_{\text{Bessel max}}) = 473 \text{ nm}$  defined by the  $NA_{\text{Bessel max}} = 0.515$  excitation used (Supplementary Fig. 11).

Such superresolution via coherent SI is well established using other algorithms<sup>13</sup>, but its appearance using the simple algorithm

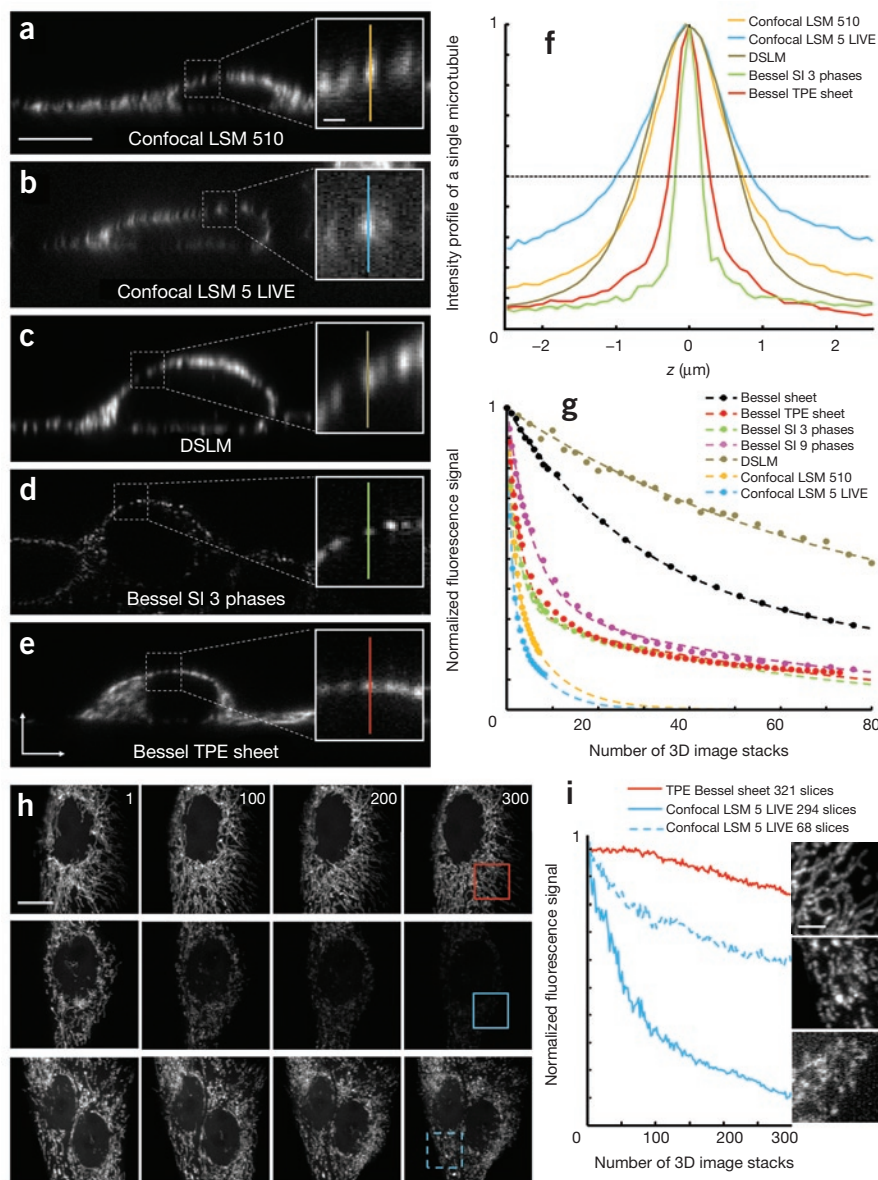
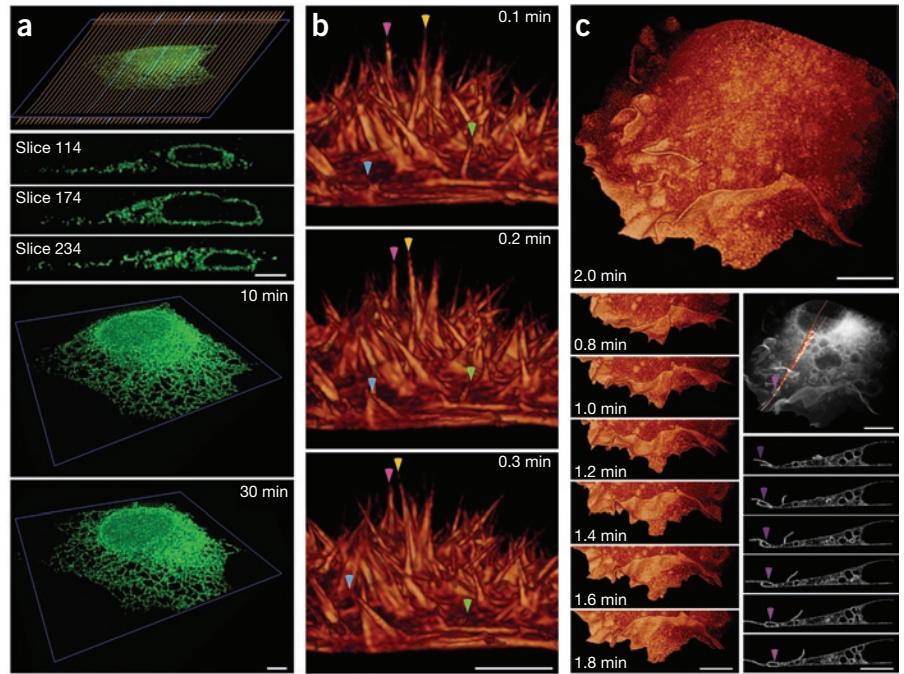


**Figure 3** | Comparisons of Bessel beam plane illumination to confocal microscopy and DSLM.

(a–e) Comparative raw image slices in a plane orthogonal to the coverslip through antibody-labeled microtubules in fixed HeLa cells: point-scanning confocal microscopy (a; Zeiss LSM 510, NA 1.2, 1 Airy unit filtering); line-scanning confocal microscopy (b; Zeiss LSM 5 LIVE, same conditions as in a); DSLM (c; NA 0.2); Bessel single harmonic SI mode (d; 3 phases,  $0.9\text{-}\mu\text{m}$  period), and Bessel TPE sheet mode (e). Scale bars,  $10 \mu\text{m}$  (inset,  $1 \mu\text{m}$ ). (f) Averages of linecuts (as shown in insets in a–e) through 40 microtubules for each method, with 50% intensity level (dashed line) shown for estimation of the FWHM. (g) Bleaching rates obtained from repeated 3D imaging of mEmerald fused to nuclear histones in fixed HeLa cells, normalized to account for differences in SNR. In addition to modes described in a–e, Bessel linear sheet and Bessel SI multiharmonic 9-phase modes are included. Dashed lines represent a double exponential fit. (h) Maximum-intensity projections of mitochondria in live LLC-PK1 cells for four image volumes as numbered at top from a series of 300 such volumes acquired by Bessel TPE sheet mode (top; 321 images per volume), confocal LSM 5 LIVE (middle; 294 images per volume) and confocal LSM 5 LIVE (bottom; 68 images per volume). Scale bar,  $10 \mu\text{m}$ . (i) Photobleaching curves extracted from the data in h, with  $10 \mu\text{m} \times 10 \mu\text{m}$  intensity-renormalized insets extracted from the boxed sub-region shown in the 300<sup>th</sup> volume in each case, showing mitochondrial fragmentation under confocal imaging. Scale bar,  $3 \mu\text{m}$ .

of equation (1) and the incoherent illumination pattern illustrated in Supplementary Figure 12 was unexpected. Nevertheless, images of ordered clusters of 304-nm-diameter fluorescent beads in a submonolayer spread (Supplementary Fig. 14) and disordered 3D

**Figure 4** | Three-dimensional isotropic imaging of live-cell dynamics. **(a)** Images of ER in a live U2OS cell, visualized in the Bessel multiharmonic 9 phase SI mode, over 45 image volumes: representation of a subset of the 321 image planes (brown lines) comprising each volume (top); images from three indicated image planes; and image volumes after 10 and 30 min of observation. **(b)** Filopodia at the apical surface of a live HeLa cell, visualized in the Bessel TPE sheet mode over three consecutive image volumes from 100 such volumes taken at 6-s intervals. Filaments that wave (magenta and yellow arrowheads), extend outward (cyan arrowhead) or retract inward (green arrowhead) are marked. **(c)** African green monkey kidney cell (COS-7) transfected with plasmids encoding mEmerald-c-Src, demonstrating retrograde flow of membrane ruffles (left) and vacuole formation by macropinocytosis (right; arrowheads) in an exemplary plane in a translucent cell view (top). All data were extracted from 73 image stacks taken at 12-s intervals. Scale bars, 5  $\mu\text{m}$  (a,b) and 10  $\mu\text{m}$  (c).



groups of 352-nm-diameter beads (**Supplementary Fig. 15** and **Supplementary Video 1**) confirmed the faithful reproduction of sample structure beyond the axial diffraction limit dictated by the excitation NA alone.

One problem with the single-harmonic SI sectioning algorithm is that the background fluorescence generated by the Bessel side lobes lowers the contrast in the three images of the imposed pattern, leading to a final image with reduced SNR. One can improve the contrast by using a single harmonic pattern with a period far beyond the  $\lambda/(2NA_{\text{detect max}})$  Abbe limit of the detection objective<sup>14</sup> but at the expense of proportionally poorer optical sectioning capability<sup>12</sup>. An alternative that attains both high SNR and axial resolution is to use a multiharmonic excitation pattern (**Supplementary Fig. 16**) generated by stepping the beam at a fundamental period larger than  $\lambda/(NA_{\text{Bessel max}})$ . To create a single SI image with a pattern having  $H$  harmonics, we again used equation (1), except with  $N \leq H + 2$  images, each with the pattern phase shifted by  $2\pi/N$  relative to its neighbors. Although the axial resolution of this multiharmonic SI mode (**Supplementary Fig. 17**) was slightly less (0.29  $\mu\text{m}$  FWHM for  $N = 9$  phases; **Supplementary Fig. 8**) than in the single harmonic case, images of fixed and living cells (**Fig. 2d,f** and **Supplementary Video 2**) still exhibited isotropic 3D resolution and improved SNR (**Supplementary Fig. 18**), albeit at the cost of more data frames required per image plane and thus lower speed.

### Two-photon Bessel beam plane illumination microscopy

In addition to this speed penalty, both SI modes still generate some excitation beyond the focal plane (**Supplementary Figs. 12** and **16**) and were thus not optimally efficient in their use of the photon budget. We addressed both these issues by using two-photon excitation (TPE), which suppresses the Bessel side lobes<sup>15</sup> and allowed us to obtain a thin light sheet (0.5  $\mu\text{m}$  FWHM) even with a continuously swept beam. As a result, we achieved high axial resolution (**Supplementary Figs. 7** and **8**) and minimal out-of-focus excitation

(**Supplementary Fig. 5**) in fixed and living cells (**Fig. 2e,g**) with only a single image per plane. Some improvement was possible with TPE SI (**Supplementary Figs. 7, 8, 11** and **19**), but we preferred the faster TPE sheet mode for live-cell imaging.

### Comparisons with confocal microscopy and DSLM

As confocal microscopy remains the workhorse for 3D cellular imaging and as DSLM is the standard for plane illumination with Gaussian beams, we compared both techniques with the various modes of Bessel beam plane illumination. Image slices in a plane orthogonal to the coverslip through 3D image stacks of Alexa Fluor 488-labeled microtubules in HeLa cells (Online Methods) demonstrated the comparative axial resolution of a high-resolution (NA 1.2) point-scanning confocal microscope (Zeiss LSM 510), a high-speed line scanning confocal instrument (Zeiss LSM5 LIVE), DSLM (NA 0.2), the Bessel beam single-harmonic SI mode and the Bessel beam TPE swept sheet mode (**Fig. 3a–e**). The longitudinal extent of the Gaussian beam used for DSLM in **Figure 3c** was similar to that of the Bessel beams in **Figure 3d,e**. The two Bessel modes (**Fig. 3d,e**) demonstrated a clear reduction in out-of-focus haze as well as superior axial resolution. Indeed, averages of 40 axial linecuts through individual microtubules (**Fig. 3f**) by each method and corresponding bead measurements (**Supplementary Fig. 8**) revealed substantially narrower axial FWHM (**Supplementary Table 1**) for the single-harmonic SI ( $\sim 2.5\times$  to  $5.7\times$ ) and TPE sheet modes ( $1.4\times$  to  $3.7\times$ ), respectively. As expected, deconvolution using a bead-measured confocal PSF and theoretical PSFs for DSLM and the various Bessel modes yielded sharper, higher-contrast images in all cases (**Supplementary Fig. 20**), but did not alter the superior axial resolution of the Bessel images relative to the DSLM or confocal ones.

To compare relative photobleaching rates without the complication of diffusion-induced recovery, we repeatedly imaged monomeric (m)Emerald-labeled histones in the nuclei of fixed

rather than live HeLa cells over a 3D volume of equal size by each method (Fig. 3g). After normalizing for small differences in the SNR (Online Methods), we acquired  $\sim 5\times$  more image stacks for the single-harmonic and multiharmonic SI modes than for either confocal instrument before bleaching to 20% of the original signal, thanks to the tighter excitation confinement near the focal plane for the Bessel methods. However, neither the SI mode nor the linear-sheet mode performed as well as DSLM, presumably for the same reason; the excitation tails arising from the Bessel side lobes led to greater out-of-focus excitation. This underscores the importance of selecting  $NA_{\text{Bessel min}}$  carefully to craft a Bessel beam only as long as necessary to cover the desired field of view (Supplementary Fig. 10). Lastly, although the TPE sheet mode yielded a  $\sim 3\times$  thinner light sheet than DSLM, its bleaching rate was only comparable to the SI modes, perhaps because of bleaching mechanisms intrinsic to TPE.

Advantages of the Bessel TPE sheet mode became clear during long-term imaging of mitochondrial dynamics in living LLC-PK1 cells (Figs. 3h,i and Supplementary Video 3): even after acquiring 300 three-dimensional image stacks, each composed of 321 image planes (96,300 images), more than 80% of the initial fluorescence intensity remained as did the original string-like morphology of the mitochondria (Fig. 3i). In contrast, after imaging a similar cell using the LSM5 LIVE confocal system under comparable conditions (Supplementary Table 2) of SNR, image volume, voxel size and speed (10 s per stack, 10 s rest between stacks), less than 20% of the fluorescence remained, and the mitochondria were substantially fragmented, which is indicative of phototoxicity. Even after further minimizing the photon exposure by restricting the vertical field of view (17  $\mu\text{m}$  versus 40  $\mu\text{m}$ ) and doubling the  $z$  step (0.25  $\mu\text{m}$  versus 0.125  $\mu\text{m}$ ), we still observed extensive fragmentation, even though neighboring, unexposed cells showed no signs of similar damage.

### 3D isotropic imaging of living cells

The improved confinement of the excitation to the vicinity of the focal plane made possible by Bessel beam plane illumination led to improved axial resolution and reduced photobleaching and phototoxicity, enabling extended observations of living cells with isotropic resolution at high volumetric frame rates (Supplementary Table 3). For example, in the linear multiharmonic SI mode, we followed the evolution of the endoplasmic reticulum (ER) in a live human osteosarcoma cell (U2OS) over 45 min at 1 stack  $\text{min}^{-1}$  with  $\sim 0.3 \mu\text{m}$  axial resolution despite the fact that over 300 image slices were required to construct each stack (Fig. 4a and Supplementary Video 4).

Even longer duration observations were possible in the TPE sheet mode. For example, we recorded 100 three-dimensional image stacks detailing the dynamics of numerous actin-based<sup>16</sup> filopodia on the apical surface of a HeLa cell (Fig. 4b and Supplementary Video 5). The imaging speeds we achieved (51.4 image planes  $\text{s}^{-1}$ , 6 s stack interval; Supplementary Video 5) enabled us to visualize even this complex, rapid 3D cellular process with sufficient time resolution. In another case (Fig. 4c), we imaged the retrograde flow of membrane ruffles formed at the leading edge of an African green monkey kidney cell (COS-7). Such ruffles surround and engulf extracellular fluid to create large intracellular vacuoles, a process known as macropinocytosis<sup>17</sup>, which we observed in a time series of image slices through the cell

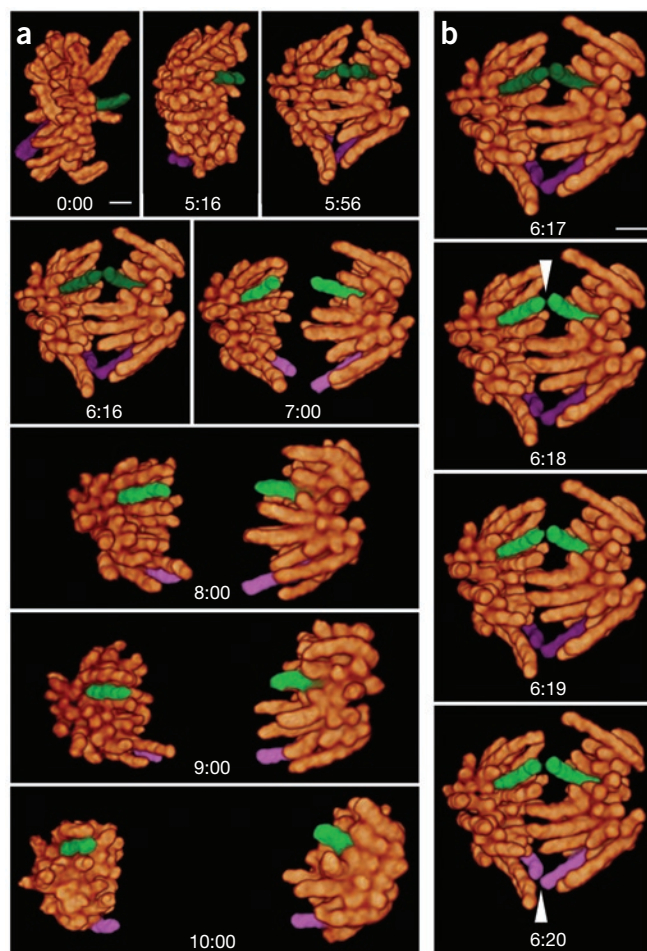


**Figure 5** | High-speed volumetric imaging of chromosomes in mitosis. (a) Eight image volumes from a series of 200 such volumes depicting mitosis in a LLC-PK1 cell transfected with plasmids encoding mEmerald-histone H2B and imaged in the Bessel TPE sheet mode. Each volume, composed of 200 image planes, was acquired in 1.0 s. The rest interval between stacks varied from 20 s in metaphase and telophase to no rest in early anaphase, to expend more of the photon budget at the points of most rapid evolution. Two chromatids (green and purple) are traced through the series. (b) Four consecutive image volumes from the series, during the fast imaging period in anaphase, in which the two chromatids separate (arrowheads). Times indicate min:s. Scale bars, 5  $\mu\text{m}$ .

(Fig. 4c). The visualization of these processes in four-dimensional spatiotemporal detail ( $0.12 \mu\text{m} \times 0.12 \mu\text{m} \times 0.15 \mu\text{m} \times 12.3 \text{ s}$  stack interval) across 15 min (73 stacks; Supplementary Video 6) cannot currently be achieved with other fluorescence microscopy techniques to our knowledge.

For sufficiently bright samples, the 10–35 MHz pixel rate of electron-multiplying charge-coupled device (EMCCD) cameras becomes a limiting factor. To achieve even higher imaging speeds, we substituted a 125 MHz scientific complementary metal oxide semiconductor (sCMOS) camera into the microscope. To exploit the full speed of the camera, we placed a third galvanometer at a plane conjugate to the rear pupil of the detection objective and tiled several image planes across the width of the sCMOS sensor, which were then read out in parallel (Supplementary Fig. 21 and Online Methods). With this faster configuration, we studied the 3D dynamics of chromatid separation in early anaphase in the TPE sheet mode at

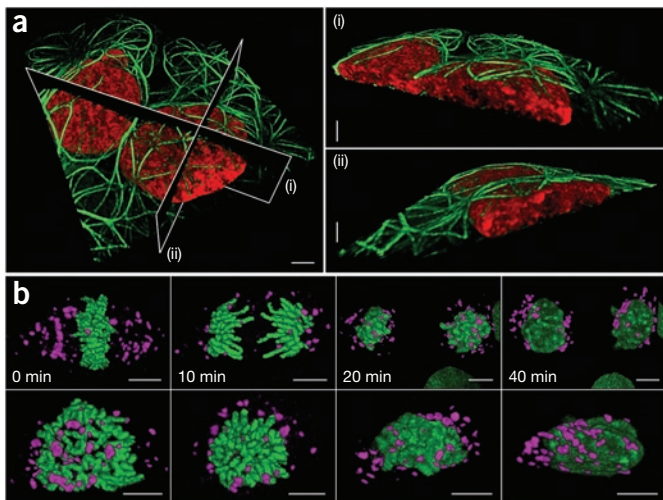


**Figure 6** | Three-dimensional isotropic imaging of protein pairs. (a) Two-color volume rendering acquired in the 9 phase multiharmonic SI mode of microtubules (green) and nuclei (red) in a pair of live U2OS cells transfected with plasmids encoding mEmerald-MAP4 and tdTomato-histone H2B. Images on the right show slices through the cell along the planes shown in the image on the left. (b) Evolution of the Golgi apparatus (magenta) during mitosis of a live LLC-PK1 cell, with views parallel (top) and perpendicular (bottom) to the mitotic plane, showing partial fragmentation in metaphase and anaphase and eventual recondensation in telophase. The Golgi and chromosomes (green) are visualized via mEmerald-Mann II and mEmerald-histone H2B fluorescence, respectively, and were manually segmented for these images. Scale bars, 5  $\mu\text{m}$ .

rates of 1 volume  $\text{s}^{-1}$  (Fig. 5 and Supplementary Video 7). Even at the intensities we used to reach these imaging rates, the excitation did not arrest mitosis. We also observed intracellular trafficking of vesicles in a COS-7 cell over 7,000 frames acquired in a single plane at 137 frames  $\text{s}^{-1}$  (Supplementary Video 8).

### 3D live-cell imaging of protein pairs

A key advantage of fluorescent proteins is that their spectral diversity permits investigation of the dynamic interactions between multiple proteins in the same living cell. For example, using mEmerald and tandem dimer (td)Tomato we performed two-color live imaging of microtubules surrounding a pair of nuclei in U2OS cells using the linear, nine-phase multiharmonic SI mode (Fig. 6a and Supplementary Video 9). However, the need for  $N$  frames of different phase per image plane limits the use of Bessel SI to processes that evolve on a scale that matches the time required to collect frames at the desired spatial resolution. This limitation does not apply to fixed cells, for which the linear SI mode is preferred, owing to its superior axial resolution and the availability of more fluorescent dyes and fluorescent proteins for protein specific labeling. For example, we performed three-color, isotropic 3D imaging of the actin cytoskeleton, the nuclear envelope and nuclear histones in a fixed LLC-PK1 cell labeled with a combination of exogenous dyes and endogenous fluorescent proteins (Supplementary Fig. 22 and Supplementary Video 10).

For imaging multiple proteins exhibiting faster dynamics, the TPE sheet mode is necessary. But this presents its own challenges: orange or red fluorescent proteins such as tdTomato and mCherry do not have the same TPE brightness and photostability of green fluorescent proteins such as enhanced (E)GFP or mEmerald and require a second

ultrafast light source because the time required to retune and realign a single source is prohibitive for live-cell imaging (Supplementary Fig. 23 and Supplementary Video 11). Fortunately the 3D isotropic resolution of the Bessel TPE sheet mode permits multiple proteins tagged with the same fluorescent protein to be imaged simultaneously as long as they are known a priori to be spatially segregated. For example, with two mEmerald-tagged fusions, we documented (Fig. 6b and Supplementary Video 12) the fragmentation of the Golgi apparatus between metaphase and anaphase, as identified by chromosome morphology and subsequent re-constitution of Golgi around the daughter nuclei in telophase.

### DISCUSSION

As currently configured, our Bessel beam plane illumination microscope offers 3D isotropic resolution down to  $\sim 0.3 \mu\text{m}$  and the ability to acquire hundreds of 3D image stacks from single living cells at speeds of nearly 200 image planes per second. We envision several improvements. First, substantially greater light collection making still better use of the photon budget would be obtained by using a detection objective of NA 1.0 or greater. Although mechanical constraints would thereby force the use of a lower-NA excitation objective and thus lead to a somewhat anisotropic PSF, the volumetric resolution would remain similar because the slight loss of axial resolution would be offset by the corresponding transverse gain.

Another issue is that the SI algorithm in equation (1) is photon-inefficient as it achieves high axial resolution by removing substantial signal encoded in the zero frequency component of the applied modulation. A better alternative would be to use the algorithms of 3D superresolution SI<sup>18</sup>, which assign the sample spatial frequencies downmodulated by all bands of the excitation to their appropriate positions in an expanded frequency space. By doing so, shorter exposure times and fewer phases may be needed to record images of acceptable SNR, making linear Bessel SI a more viable option for high-speed multicolor imaging. In addition, resolution could be extended to the sum of the excitation and detection MTF limits in each direction, an argument in favor of using three mutually orthogonal objectives in a future system. The marriage of Bessel beam plane illumination and 3D SI may permit the latter to be applied to thicker, more densely fluorescent specimens than the conventional wide-field approach while more efficiently using the photon budget.

Highly inclined, objective-coupled sheet illumination<sup>19</sup> has been used to image single molecules in thicker regions of the cell where autofluorescence and out-of-focus excitation would be otherwise prohibitive under wide-field illumination. With the thinner light sheets of Bessel beam plane illumination, only in-focus molecules would be excited whereas out-of-focus ones would not be prematurely bleached. As such, it would be well-suited to live-cell 3D particle tracking<sup>20</sup> and fixed cell photoactivated localization microscopy<sup>1</sup>.

At the other extreme, the TPE sheet mode may be equally well suited to imaging large, multicellular specimens that are now the province of DSLM<sup>7,14</sup> because it combines the self-reconstructing property of Bessel beams<sup>10,11</sup> with the improved depth penetration in scattering media characteristic of TPE. In addition to large-scale 3D anatomical mapping with isotropic resolution, at high frame rates it might be fruitfully applied to the *in vivo* imaging of activity in populations of neurons<sup>21</sup>.

## METHODS

Methods and any associated references are available in the online version of the paper at <http://www.nature.com/naturemethods/>.

Note: Supplementary information is available on the Nature Methods website.

## ACKNOWLEDGMENTS

We thank D. Cabaniss and S. Bassin for machining services, H. White and S. Michael for sample preparation; A. Arnold for confocal microscopy support; H. Shroff for early instrumentation development; and M. Gustafsson, L. Shao, R. Fiolka, P. Keller and N. Ji for valuable discussions. mCerulean3 was a gift of M.A. Rizzo (University of Maryland) and Neptune was a gift of M.Z. Lin (Stanford University). Partial support was provided by the intramural program of the National Institute of Neurological Disorders and Stroke.

## AUTHOR CONTRIBUTIONS

E.B. conceived the project and designed the instrumentation; D.E.M. wrote the instrument control program under suggestions from T.A.P., L.G. and E.B.; M.W.D. supplied plasmids, figures and guidance on cell lines and useful targets therein; T.A.P. performed initial system characterization and confocal experiments; L.G. performed two-photon measurements; L.G., C.G.G. and J.A.G. performed live-cell experiments; T.A.P., L.G., C.G.G., J.A.G. and E.B. analyzed the data; and E.B. wrote the paper with input from all authors.

## COMPETING FINANCIAL INTERESTS

The authors declare no competing financial interests.

Published online at <http://www.nature.com/naturemethods/>.

Reprints and permissions information is available online at <http://npg.nature.com/reprintsandpermissions/>.

- Lippincott-Schwartz, J. & Manley, S. Putting super-resolution fluorescence microscopy to work. *Nat. Methods* **6**, 21–23 (2009).
- Toomre, D. & Pawley, J.B. Disk-scanning confocal microscopy. in *Handbook of Biological Confocal Microscopy* 3<sup>rd</sup> edn. (ed., J.B. Pawley) 221–238 (Springer, New York, 2006).
- Zimmermann, T., Rietdorf, J. & Pepperkok, R. Spectral imaging and its applications in live cell microscopy. *FEBS Lett.* **546**, 87–92 (2003).
- Khodjakov, A. & Rieder, C.L. Imaging the division process in living tissue culture cells. *Methods* **38**, 2–16 (2006).
- Huisken, J. & Stainier, D.Y.R. Selective plane illumination microscopy techniques in developmental biology. *Development* **136**, 1963–1975 (2009).
- Huisken, J., Swoger, J., Del Bene, F., Wittbrodt, J. & Stelzer, E.H.K. Optical sectioning deep inside live embryos by selective plane illumination microscopy. *Science* **305**, 1007–1009 (2004).
- Keller, P.J., Schmidt, A.D., Wittbrodt, J. & Stelzer, E.H.K. Reconstruction of zebrafish early embryonic development by scanned light sheet microscopy. *Science* **322**, 1065–1069 (2008).
- Durnin, J., Miceli, J.J. & Eberly, J.H. Comparison of Bessel and Gaussian beams. *Opt. Lett.* **13**, 79–80 (1988).
- Lin, Y., Seka, W., Eberly, J.H., Huang, H. & Brown, D.L. Experimental investigation of Bessel beam characteristics. *Appl. Opt.* **31**, 2708–2713 (1992).
- Garcés-Chaves, V., McGloin, D., Melville, H., Sibbett, W. & Dholakia, K. Simultaneous micromanipulation in multiple planes using a self-reconstructing light beam. *Nature* **419**, 145–147 (2002).
- Fahrbach, F.O., Simon, P. & Rohrbach, A. Microscopy with self-reconstructing beams. *Nat. Photonics* **4**, 780–785 (2010).
- Neil, M.A., Juškaitis, R. & Wilson, T. Method of obtaining optical sectioning by using structured light in a conventional microscope. *Opt. Lett.* **22**, 1905–1907 (1997).
- Gustafsson, M.G.L. Surpassing the lateral resolution limit by a factor of two using structured illumination microscopy. *J. Microsc.* **198**, 82–87 (2000).
- Keller, P.J. *et al.* Fast, high-contrast imaging of animal development with scanned light sheet-based structured-illumination microscopy. *Nat. Methods* **7**, 637–642 (2010).
- Botcherby, E.J., Juškaitis, R. & Wilson, T. Scanning two photon fluorescence microscopy with extended depth of field. *Opt. Commun.* **268**, 253–260 (2006).
- Riedl, J. *et al.* Lifeact: a versatile marker to visualize F-actin. *Nat. Methods* **5**, 605–607 (2008).
- Mercer, J. & Helenius, A. Virus entry by macropinocytosis. *Nat. Cell Biol.* **11**, 510–520 (2009).
- Gustafsson, M.G.L. *et al.* Three dimensional resolution doubling in wide-field fluorescence microscopy by structured illumination. *Biophys. J.* **94**, 4957–4970 (2008).
- Tokunaga, M., Imamoto, N. & Sakata-Sogawa, K. Highly inclined thin illumination enables clear single-molecule imaging in cells. *Nat. Methods* **5**, 159–161 (2008).
- Ram, S., Prabhat, P., Chao, J., Ward, E.S. & Ober, R.J. High accuracy 3D quantum dot tracking with multifocal plane microscopy for the study of fast intracellular dynamics in live cells. *Biophys. J.* **95**, 6025–6043 (2008).
- Holekamp, T.F., Turaga, D. & Holy, T.E. Fast three-dimensional fluorescence imaging of activity in neural populations by objective-coupled planar illumination microscopy. *Neuron* **57**, 661–672 (2008).

## ONLINE METHODS

**Bessel beam plane illumination microscope.** Four lasers of excitation wavelengths 405 nm, 488 nm, 561 nm and 635 nm are expanded to a common  $1/e^2$  beam diameter of 2.0 mm and combined into a single co-linear beam using dichroic beamsplitters. An acousto-optic tunable filter (AOTF) is used to select one or more wavelengths, control intensities and provide on-off modulation for structured illumination. The combined beam is then sent to the  $x$  galvanometer.

In a separate path, the near-infrared beam from a Ti-sapphire laser passes through a Pockels cell, is expanded to a 6.0 mm  $1/e^2$  diameter and is sent through a near-infrared achromat and axicon doublet to create an annular excitation pattern<sup>22</sup> at the focal plane of the achromat. A pair of relay lenses then image the annular pattern at an outer diameter of 0.65 mm to 1.3 mm (depending on the desired NA of the eventual Bessel beam) onto the  $x$  galvanometer.

The visible or near-infrared light impinging on the  $x$  galvanometer is imaged at  $2\times$  magnification by relay lenses onto the conjugate  $z$  galvanometer, and then magnified an additional  $3\times$  by relay lenses and imaged onto a conjugate custom-fabricated annulus mask. The mask contains various transmissive annuli of differing outer and inner diameters etched into an opaque aluminum coating on a quartz substrate; each annulus defines a Bessel beam of unique central peak width and longitudinal extent (**Supplementary Figs. 1 and 2**).

With appropriate relay lenses chosen to match the diameter of the annular near-infrared excitation pattern from the achromat and axicon doublet to the diameter of the desired annulus in the mask,  $>50\%$  of the energy impinging on the mask is transmitted. Such an arrangement is needed in the two-photon mode to deliver enough average power ( $\sim 50$ – $250$  mW) to the rear pupil of the excitation objective to permit imaging at frame rates of 5–30 ms over fields of view as large as  $60\ \mu\text{m} \times 80\ \mu\text{m}$ . However, for linear excitation, a simple Gaussian beam projected onto the annulus can transmit enough power ( $\sim 5$ – $100\ \mu\text{W}$ ) to image at 10–100 ms per frame.

The spatially filtered annular beam emerging from the annulus mask is imaged via another pair of relay lenses onto the conjugate back focal plane (BFP) of water-dipping excitation objective. The light is then focused by the excitation objective to form the Bessel beam in the sample chamber.

Two different approaches are used to measure fluorescence generated by the beam in the sample. In the high-sensitivity version, light collected by the detection objective is imaged directly via a tube lens onto an EMCCD camera. In the high-speed version (**Supplementary Fig. 21**), light collected by the detection objective is first imaged by a tube lens at an intermediate image plane, where an adjustable slit crops the image in the  $y$  direction to sharply define the field of view. A pair of relay lenses transfers this image to an sCMOS camera. To exploit the full speed of the camera, a third, tiling galvanometer placed between the relay lenses at the plane conjugate to the BFP of the detection objective is rotated in discrete steps as successive planes in the specimen are scanned. As a result, several images are tiled across the width of the camera sensor and can be read out in parallel.

In general, an image at a single plane is created by using the  $x$  galvanometer to scan the Bessel beam across the focal plane of the detection objective while integrating the fluorescence signal collected by the detection objective at the camera. A 3D image stack is then acquired by repeating this process at multiple planes along the axis of the detection objective, using the  $z$  galvanometer to translate the beam while moving the detection objective by the same amount using a piezoelectric collar (100  $\mu\text{m}$  range).

The specimen is placed on a 18-mm coverslip, clamped into a custom sample holder (**Supplementary Fig. 4a**) and inserted from above into a cavity in a sample chamber filled with aqueous medium. Silicone rubber film (70–80  $\mu\text{m}$  thick) stretched over the sides of the excitation, detection and epi-illumination objectives is clamped to the sides of the sample chamber to contain the media in the sample chamber while still permitting the objectives to move with minimal resistance. The sample and holder are mounted at a  $45^\circ$  angle in the  $y$ – $z$  plane defined by the axes of excitation and detection objectives, and translated with sample stages to place the desired part of the specimen in the imaging volume. An epi-illumination objective orthogonal to the sample holder provides a conventional, low-magnification view of the sample and serves as a viewfinder.

Information on specific part numbers and vendors for all key components is given in **Supplementary Table 4**.

**Control electronics.** A control schematic for the microscope is shown in **Supplementary Figure 24**. The camera, set to internal triggering, served as the master timing source. Timing pulses from the camera triggered a field-programmable gate array (FPGA) card which generated user-defined waveforms (**Supplementary Fig. 25**) to control the hardware above. Analog outputs controlling the  $x$  and  $z$  galvanometers, the piezoelectric collar, and the tiling galvanometer were conditioned by individual scaling amplifiers to match their 16-bit resolution to the control range of each device. During linear operation (for example, Bessel single or multiharmonic SI modes), additional analog output drove the AOTF to control the intensity of each laser wavelength individually. During two-photon operation, additional outputs drove a Pockels cell and a mechanical shutter to control the intensity of the excitation or block it completely. The FPGA and image capture cards reside in a control computer with dual Hexa-core processors and 96 gigabytes of RAM (random-access memory).

**Control software.** All control software was written in LabView 2010, 64-bit version. A timing diagram is shown in **Supplementary Figure 25a** for the exemplary case of 3D data acquisition using a continuously swept beam (for example, TPE sheet mode) and the high-speed configuration with an sCMOS camera and tiling galvanometer (**Supplementary Fig. 21**). When tiling  $T$  images, a sawtooth waveform of  $T$  periods was generated for the  $x$  galvanometer over one interval of camera exposure, thereby initiating  $T$  sweeps of the Bessel beam across the field of view. At the same time, a square waveform of  $T$  periods was applied to the AOTF or Pockels cell to ensure that the excitation was delivered to the sample only during the  $T$  forward sweeps of the beam. At the beginning of each flyback, the voltages to the  $z$  galvanometer and piezoelectric collar were incremented to ensure that the Bessel beam and focal plane of the detection objective settled to the next  $z$  plane in the specimen before the next sweep commenced, and the voltage to the tiling galvanometer was incremented to ensure that the light from the next image plane fell on the next tiled section of the sCMOS sensor. After all  $T$  images were exposed, all control voltages returned to their initial state whereas all  $T$  images were read out in parallel.

In the single- and multiharmonic SI modes, the waveform for the  $x$  galvanometer was not a continuous ramp but rather a series of discrete steps (**Supplementary Fig. 25b**). At the start of each step, the AOTF or Pockels cell voltage was set low during the  $\sim 100\ \mu\text{s}$  interval required for the  $x$  galvanometer to settle to a new position but otherwise was kept high to expose the sample at a periodic set

of discrete points in the  $x$  dimension. For SI with  $N$  phases, these waveforms were repeated for  $N$  images at each  $z$  plane except that a slight offset was added to the waveform for the  $x$  galvanometer in each case to shift the exposure pattern by the desired phase.

**Beam alignment.** Precise conjugation of the  $x$  and  $z$  galvanometers and the annular mask to the BFP of the excitation objective was essential to achieve a uniform, high-quality Bessel beam across the entire image volume. Mutual conjugation of these elements was obtained by diverting the beam transmitted through the annulus mask to an inspection camera conjugated to the annulus mask and adjusting the axial positions of the various relay lenses until no motion of the annular beam was seen as the  $x$  and  $z$  galvanometers were scanned. The annulus mask was conjugated to the BFP to the excitation objective by filling the sample chamber with  $H_2O$ , replacing the epi-illumination objective with a transparent view port and adjusting the axial positions of the relay lenses between the annulus mask and excitation objective until the annular excitation pattern expanding past the focus of the excitation objective (**Supplementary Fig. 4b**) was in focus on a screen  $\sim 40$  cm beyond the view port.

Uniform intensity across the annular excitation pattern is necessary to produce a symmetric Bessel function with maximal energy in the central peak. To achieve this, the  $x$  and  $z$  galvanometers and the annulus mask were moved transversely with stages while measuring the intensity distribution at the inspection camera. For the near-infrared beam, the axicon was translated laterally to obtain a uniform annular illumination pattern before the annulus mask.

Concentricity of the final annular pattern to the rear pupil of excitation objective is also critical, as transverse misalignment at the BFP corresponds to a tilt of the plane swept by the Bessel beam relative to the focal plane of the detection objective. To achieve parallelism of these planes, the sample chamber was filled with a fluorescent dye solution, and the image of the Bessel beam recorded by the camera was monitored while the  $z$  position (**Supplementary Fig. 3**) of the annular excitation in the BFP was adjusted with mirrors until the beam was in focus across its length. The  $x$  position of the excitation was then adjusted until the beam was aligned along the  $y$  axis (perpendicular to the scan direction).

To insure that the scan plane and detection focal plane were coincident at all times, the piezoelectric collar was used to move the detection objective to several  $z$  positions throughout the image volume, and the control voltage to the  $z$  galvanometer required to achieve a focused Bessel beam at each position was recorded. From these measurements, an interpolated control waveform was calculated for the  $z$  galvanometer such that, whenever a 3D image stack was acquired, the Bessel scan plane always remained in focus as observed by the detection objective. For cases in which drift later occurred during cellular imaging, any point-like object in the sample could be used to apply a corrective offset voltage to the piezoelectric collar until symmetry was regained in the observed axial PSF.

When all of these alignment steps were completed, the PSF of the microscope was invariant throughout the entire image volume, regardless of the specific mode of operation used (**Supplementary Fig. 26**). This was essential for the validity of subsequent deconvolution and to minimize artifacts in the final 3D images.

**Bessel beam characterization.** The longitudinal extent of the Bessel beam (**Supplementary Fig. 2**) was measured directly from the image of the beam in dye solution, as above.

The  $x$ - $z$  cross-sectional profile of the beam (**Supplementary Fig. 1**) was measured by first positioning an isolated fluorescent bead to the center of the beam in the medium-filled sample chamber. Yellow-green 100-nm-diameter and 200-nm-diameter beads were used for linear and two-photon measurements, respectively. The piezoelectric collar was fixed at the position that provided an in-focus image of the bead on the camera. The  $x$  and  $z$  galvanometers then scanned the beam across the bead, and an image was recorded of the bead at each beam position. From each image, the signal integrated in a window around the bead provided a measurement of the cross-sectional intensity of the beam at a specific  $x$ - $z$  position relative to its central peak. The set of all such measurements then yielded a 2D map of the  $x$ - $z$  cross-sectional intensity profile of the beam.

**Point spread function measurements.** Two types of PSF measurements were made: 2D excitation PSFs (**Supplementary Figs. 1, 12 and 16**) and 3D overall PSFs (**Supplementary Figs. 7, 13 and 17**). Each used 100-nm or 200-nm fluorescent beads, as above. For all excitation PSFs, the detection objective remained focused on the bead and only the Bessel beam excitation pattern was moved in  $x$  and  $z$  dimensions. Each pixel in the resulting PSF then represented the integrated signal around the bead at the corresponding position of the excitation pattern. In contrast, for all overall PSFs, the detection objective was moved in concert with the  $z$  motion of the excitation pattern, keeping the Bessel beam in focus at all times. The image of the bead obtained at each  $z$  plane then gave the  $x$ - $y$  component of the overall PSF at that plane. In all cases, the experimental modulation transfer functions (**Supplementary Figs. 11, 12, 13, 16 and 17**) were calculated from the absolute magnitude of the Fourier transform of the corresponding experimental PSF.

**Theoretical point spread functions.** All theoretical PSFs were calculated using a vector model of diffraction by an ideal lens of arbitrary NA<sup>23</sup>. In particular, the excitation PSF of a single Bessel beam (**Supplementary Fig. 1**) was calculated using integrals  $I_1$ ,  $I_2$  and  $I_3$  in reference 23, except with the lower limit of integration changed from zero (that is, integration over the full solid angle defined by the NA) to the minimum illumination angle defined by the inner annulus diameter at the rear pupil. The two-photon single Bessel excitation PSF was calculated in the same manner, except using the longer excitation wavelength and squaring the result at the end. The theoretical wide-field PSF (**Supplementary Fig. 7**) was calculated via integration over the full solid angle defined by the 0.8 NA of the detection objective.

The linear and two-photon theoretical sheet excitation PSFs were calculated by integrating the corresponding single Bessel beam PSFs along the  $x$  scan axis. The corresponding overall PSFs (**Supplementary Fig. 7**) were given by the products of these excitation PSFs with the wide-field detection PSF.

The linear (**Supplementary Figs. 12 and 16**) and two-photon theoretical SI excitation PSFs were calculated by summing a periodic series of single Bessel beam PSFs, each offset by the stated period along the  $x$  axis relative to its nearest neighbors. The sum extended  $10\ \mu\text{m}$  beyond the plotted field of view to account for the contribution of side lobes from beams outside the field.

The linear and two-photon theoretical SI overall PSFs (**Supplementary Fig. 7**) for  $N$  phases were calculated by creating  $N$  copies of the SI excitation PSF, each offset by  $1/N$  of the SI excitation period along the  $x$  axis relative to one another, combining these

copies according to equation (1), and then multiplying the result by the wide-field detection PSF.

**Live-cell imaging.** Cells were imaged at 37 °C in DMEM with HEPES containing no phenol red. Temperature was maintained with a closed-loop system consisting of three Kapton heater tapes affixed to the exterior of the sample chamber, a resistance temperature detection probe inserted in the imaging medium and a proportional-integral-differential controller. After stabilization at 37 °C, PSFs measured from 100-nm beads were used to determine the offset voltage to the piezoelectric collar needed to align the focal plane of the detection objective to the scan plane of the Bessel beam. Cells could remain in the chamber more than 3 h and still undergo mitosis.

**Cell imaging parameters.** The parameters used to acquire the cellular images in **Figures 2–6** and **Supplementary Videos 2–12** are summarized in **Supplementary Tables 2** and **3**.

**Image deconvolution and display.** Deconvolution of all images was performed in Amira version 5.3 (Visage Imaging) using an iterative maximum-likelihood image restoration algorithm. Owing to the good agreement observed between the experimental and theoretical PSFs in all cases, the appropriate noise-free theoretical PSF, resampled to match the voxel size of the data, was used as the kernel for deconvolution. Typically, convergence to better than 2% was obtained in 12–15 iterations.

Maximum intensity projections and volume renderings were performed using the ProjectionView and Voltex functions in Amira.

**Photobleaching measurements.** For the image shown in **Figure 3g**, fixed HeLa cells transfected with plasmids encoding mEmerald–histone H2B were used. For consistency, a 60  $\mu\text{m} \times 60 \mu\text{m} \times 40 \mu\text{m}$  imaging volume and a voxel of 0.13  $\mu\text{m} \times 0.13 \mu\text{m} \times 0.10 \mu\text{m}$  was used for each method, and excitation power and detector gain was adjusted to typical levels in each case yielding 3D image stacks of similar SNR in typical acquisition times.

For each method, a selected volume encompassing a nucleus was repeatedly imaged, until the initial fluorescence intensity dropped by at least 80%. The integrated fluorescence in a 10  $\mu\text{m} \times 10 \mu\text{m} \times 10 \mu\text{m}$  subvolume was then calculated for each image stack in the series. An initial photobleaching curve was obtained by plotting this integrated fluorescence, normalized to that in the first stack, across all stacks.

As the bleaching rate will increase as more signal is demanded from each image stack, comparison across methods requires that these results be normalized to account for small differences in SNR as well<sup>24</sup>. The signal for the initial stack was estimated for each method by: (i) Fourier transforming the raw stack in 3D; (ii) applying a mask to remove all frequency components beyond the Abbe limit; (iii) transforming back to obtain a filtered image stack; (iv) applying a mask to select only the top 20% brightest voxels; and (v) denoting the average value of these brightest voxels as the signal  $S$ . The noise for the initial stack for each method was estimated by: (vi) subtracting the raw and filtered 3D image stacks to obtain a noise stack; (vii) applying the same mask from item iv above to select only a subset of noise voxels; and (viii) denoting the RMS value of these voxels as the noise  $N$ .

Finally, the  $x$  axes of the initial photobleaching curves were rescaled according to the relative initial SNR values obtained using each technique.

**Coverslip preparation.** We cleaned 18-mm-diameter coverslips via immersion for 12 h in a continuously stirred 1:1:5 mixture by volume of 50%  $\text{H}_2\text{O}_2$ , 30%  $\text{NH}_4\text{OH}$  and ultrapure  $\text{H}_2\text{O}$ . Coverslips were then rinsed with ultrapure  $\text{H}_2\text{O}$ , dipped in  $\text{CH}_3\text{OH}$  and passed briefly through a gas flame. Coverslips destined for cell culture were coated with 10  $\mu\text{g ml}^{-1}$  fibronectin in 1 $\times$  PBS (pH 7.4), overnight at 4 °C.

**Preparation of fluorescent bead samples.** We pipetted 20  $\mu\text{l}$  of a 10  $\text{mg ml}^{-1}$  solution of poly(D-lysine) hydrobromide in  $\text{H}_2\text{O}$  onto an uncoated, cleaned coverslip, and allowed it to dry for 30 min. After rinsing in  $\text{H}_2\text{O}$ , 20  $\mu\text{l}$  of a solution of fluorescent beads of the desired concentration and bead diameter was pipetted onto the coverslip and dried on a hot plate at 40 °C. Finally, unattached beads were removed by repeated washing in ultrapure  $\text{H}_2\text{O}$ .

**Cell culture and transfection.** LLC-PK1, U2OS, HeLa or COS-7 (American Type Culture Collection) cells were grown to ~55–85% confluency in Dulbecco's modified medium with high glucose and no phenol red supplemented with 15% FBS and 4 mM L-glutamine. Cells were transiently transfected with an Amaxa Nucleofector 96-well shuttle system per the manufacturer's guidelines, using the following Nucleofector programs for each of the different cells lines: Kit SEM program FF-138 (LLC-PK1); Kit SG program EH-100 (U2OS); Kit SEM program CN-114 (HeLa); and Kit SEM program FF-104 (COS-7). Cells were then grown on fibronectin-coated coverslips for 24–30 h after transfection before fixation or live-cell imaging.

**Cell fixation.** Cells were fixed for 15 min at 37 °C in a solution of 4% paraformaldehyde and 0.1% glutaraldehyde (pH 7.4). After fixation cells were rinsed 3 $\times$  in PBS.

**Phalloidin staining.** Fixed cells were permeabilized in 0.5% Triton X-100 in PBS for 10 min and then rinsed 3 $\times$  with 0.1% Triton X-100 in PBS for 5 min each followed by Abdil blocking buffer (BRB80 (80 mM PIPES, 1 mM EGTA and 1 mM  $\text{MgCl}_2$ ; pH 6.9) with 0.1% Triton X-100 and 2% (w/v) BSA) for 10 min. Cells were then incubated in a 1:40 mixture of fluorescent phalloidin (1  $\mu\text{g ml}^{-1}$ ) in Abdil for 20 min, rinsed 3 $\times$  with 0.1% Triton X-100 in PBS for 5 min each and finally rinsed in PBS.

**Alpha-tubulin staining.** Cells were first extracted in BRB80 with 4 mM EGTA and 0.5% Triton X-100 for 30 s and then fixed. After three rinses with 0.1% Triton X-100 in PBS for 5 min each, a quenching solution of 1  $\text{mg ml}^{-1}$  sodium borohydride in PBS was added for 10 min, followed by Abdil for 10 min. Primary antibodies to  $\alpha$ -tubulin (clone DM1A) were then added for 30 min and, after washing with BRB80-T, incubated with fluorescent secondary antibody overnight at 4 °C.

22. Bélanger, P.A. & Rioux, M. Ring pattern of a lens-axicon doublet illuminated by a Gaussian beam. *Appl. Opt.* **17**, 1080–1088 (1978).
23. Richards, B. & Wolf, E. Electromagnetic diffraction in optical systems. II. Structure of the image field in an aplanatic system. *Proc. R. Soc. Lond.* **253**, 358–379 (1959).
24. Murray, J.M. Evaluating the performance of fluorescence microscopes. *J. Microsc.* **191**, 128–134 (1998).